

Atomic and Kelvin Force Microscopy Applied on Hydrogenated Diamond Surfaces

B. Rezek^{*,**}

Diamond Research Center, AIST,
Central 2, 1-1-1 Umezono, Tsukuba 305-8568, Japan

(Received 29 March 2005; accepted 8 June 2005)

Correlation of atomic force (AFM) and Kelvin force microscopy (KFM) across hydrogenated (conductive), oxidized (highly resistive), and metallized (gold and aluminum) surface regions is used to deduce local surface work functions, Fermi energy levels, surface states, space charges, and accumulation and depletion regions on these surfaces and at their junctions and interfaces. Electronic properties and morphology of hydrogenated diamond surfaces are locally modified using negatively biased AFM cantilevers, which leads to insulating nanoscale patterns scribed into the diamond surfaces. The results, resolution and accuracy of the AFM and KFM measurements are discussed in detail, including the influence of plasma hydrogenation, illumination and humidity. Combination of AFM patterning and KFM visualization of electronic properties enables local examination and in-situ control of in-plane gate transistor devices realized on diamond. Providing an invaluable insight into the unique properties of diamond, the AFM and KFM techniques contribute to understanding, improving and initiating new concepts for diamond-based devices.

1. Introduction

From the material point of view, diamond is a wide-band-gap semiconductor with electronic properties that can be varied from insulating (in the case of intrinsic diamond) to conductive using boron (p-type)⁽¹⁾ or phosphorous (n-type) doping.⁽²⁾ In addition to bulk properties, a high p-type surface conductivity has been detected on hydrogen-terminated diamond surfaces.⁽³⁾ Due to a strong electric dipole of C-H bonds, the hydrogen-terminated surfaces also exhibit a negative electron affinity up to -1.3 eV^(4,5) and hydrophobic wetting properties.

*Corresponding author: e-mail: bohuslav.rezek@aist.go.jp

**On leave from: Institute of Physics ASCR, Cukrovarnická 10, 162 53 Prague, Czech Republic

Consequently, it is not surprising that surface conductivity has received much attention for applications in electronic^(6,7) and biosensor devices.^(8,9) However, its nature and origin are still not fully understood. As it is generated by hydrogen termination of the surfaces (obtained for instance by exposing diamond at 500–850°C to a hydrogen plasma), theories have been proposed ranging from hydrogen-induced surface acceptors⁽¹⁰⁾ to an acceptor subsurface region created by incorporation of hydrogen⁽¹¹⁾ or to a buried acceptor layer.⁽¹²⁾ Observations of the strong influence of atmospheric adsorbates on the surface conductivity have led to the proposal and development of a transfer doping model.^(13–18) In this model a hole accumulation in the valence band is generated at the diamond surface by the transfer of electrons through the C-H surface dipole into the electrochemical system of the adsorbate layer. In spite of corroboration by many experiments, little is known about the details of this phenomenon.

Without hydrogen termination the diamond surface becomes highly resistive.^(3,10) This enables realization of in-plane electronic devices by selective control of surface termination. On a microscopic level, surface termination can be modified by photo- or electron beam lithography with a subsequent exposure to oxygen plasma⁽⁷⁾ or using atomic force microscopy (AFM).^(19–21) AFM has the advantage that, in principle, no lithographic masks are required and no radiation damage occurs. In reality, AFM patterning is usually combined with common lithographic processing for device fabrication.⁽²²⁾

In AFM, electrically insulating patterns are formed on diamond surfaces by applying negative bias voltages on the AFM cantilever which scans the surface. Formation of the patterns is attributed to anodic oxidation, which is a well-established process on silicon.⁽²³⁾ Its mechanism on diamond still needs to be elucidated.

On diamond, the anodic process was observed to result both in deposition^(19,20) and etching^(21,22,24) of the patterns. Appearance of the patterns in height or depth depends on the interactive forces in contact and noncontact AFM measurements.⁽²¹⁾ These measurements indicated that there may be a selective adsorption of air moisture on the patterns in sub-nanometer thickness.

Understanding these and other unique properties of diamond⁽²⁵⁾ is essential to design and control of diamond-based devices. Data scattering of surface electronic properties reported in the literature^(11,26,27) indicates that the structure and quality of diamond surfaces needs a closer investigation, in particular on a microscopic level.

Here, scanning probe techniques, of which scanning tunnelling microscopy (STM)⁽²⁸⁾ and atomic force microscopy⁽²⁹⁾ are the main representatives, stand out as versatile tools that can characterize and also modify^(19,21,30) surface microstructure and electronic properties with high resolution. This can be done in vacuum, in air, as well as in other environments.

Studies by STM showed, for instance, domains of various surface reconstructions including some amorphous regions on as-deposited diamond surfaces.^(31,32) Unlike the detection of tunnelling currents in STM, AFM senses forces between the tip and the sample^(29,33) which allow measurements on both conductors and insulators. This is especially useful for studies on diamond surfaces, the conductivities of which can vary from conductive to highly resistive. By measuring various forces, or more generally, interactions, AFM allows not only characterization of surface morphologies, but also the detection of surface potentials, magnetic domains, and many other features. This enables direct correlation of electronic and morphological features on a microscopic level.⁽³⁴⁾

In particular, detection of surface potentials by Kelvin force microscopy (KFM)^(35–40) has been established as a valuable technique for imaging and evaluation of surface charges,^(30,41) space charge regions at material junctions⁽⁴¹⁾ or grain boundaries,⁽³⁹⁾ surface work functions,^(35,38) and even molecular patterns⁽⁴²⁾ and DNA molecular chains⁽⁴³⁾ with high lateral resolution. On hydrogenated diamond surfaces, KFM can be applied to deduce the surface Fermi level energy,^(17,24) which is a crucial parameter for understanding the origin of the surface conductivity, as well as to investigate surface terminations, space charge regions, and functionality of diamond in-plane devices.^(20,22,44) Nevertheless, a careful evaluation of KFM data and measurement conditions is required to obtain reliable information about material properties.

In this article, use of AFM and KFM on diamond surfaces is reviewed and discussed in detail. KFM potential profiles and images across metallic, hydrogenated and oxidized regions are used to obtain information about the local electronic properties of diamond surfaces. On the basis of these data we discuss the method, resolution and accuracy of the KFM technique itself as well as the influence of illumination and other ambient conditions on the potential profiles. At the same time, surface morphologies are characterized by AFM and correlated with the KFM images.

AFM is also used for the modification of hydrogenated diamond surfaces. Negatively biased AFM cantilevers are used to locally remove hydrogen termination, which results in the formation of electrically insulating patterns and the nanoscale etching of diamond surfaces. The microstructure and electronic properties of the patterns are characterized using the AFM cantilever as a point contact. The effect of contact and noncontact AFM on the appearance of the patterns is discussed by considering different electrical potentials and selective moisture adsorption on the patterns.

2. Materials and Methods

2.1 Hydrogenated diamond samples

Two types of diamond surfaces were used in this study: 1) undoped diamond layers grown by hot-filament or microwave plasma chemical vapor deposition (CVD) on <100> Ib diamond substrates, and 2) natural <100> IIa diamond substrates which were hydrogenated in a microwave plasma.

The hot-filament process parameters were as follows: 1.2% dilution of CH₄ in H₂, tungsten filament temperature 2200°C, sample temperature 690°C, filament-sample distance 6 mm, pressure 50 mbar, gas flow 100 sccm. The microwave CVD process parameters were as follows: sample temperature 800°C, power 750 W, gas pressure 25 Torr, hydrogen flow 400 sccm, methane (CH₄) flow 0.2 sccm. The as-grown microwave CVD samples as well as natural IIa substrates were cleaned in a 3:1 mixture of sulfuric (H₂SO₄) and nitric acid (HNO₃) by boiling at 250°C for 30 min and were rehydrogenated by a microwave plasma under following conditions: 5–30 min at 40 Torr, 800 W, sample temperature 850°C. Samples were cooled down to room temperature in hydrogen atmosphere.

Photo- and electron beam lithography followed by oxygen plasma treatments (d.c. power 300 W, 1 min, O₂ partial pressure 1 mbar) were used to fabricate isolated hydrogen-terminated patterns and in-plane gate transistor structures.^(7,22) The hydrogen-terminated regions were contacted by thermally evaporated gold (ohmic contact) or aluminum (Schottky

contact). Structural and electronic properties of diamond surfaces were then characterized by AFM and KFM under ambient conditions.

2.2 Atomic force microscopy

AFM was operated in contact (c-AFM) and noncontact (nc-AFM) regimes.⁽²⁹⁾ Primarily, the surface morphologies are represented by nc-AFM images of surface height. In the noncontact regime, the AFM is also sensitive to all kinds of long-range interactions including electrostatic, which makes it an ideal arrangement for spatially resolved KFM measurements.

2.3 Kelvin force microscopy

The Kelvin probe technique is a well-known method of determining the difference between the work functions of a reference electrode and the sample surface by measuring contact potential differences (CPD).⁽⁴⁵⁾ In general, the CPD depends on a variety of parameters such as the work function, adsorption layers, oxide layers, dopant concentration in semiconductors, and temperature changes on the sample.⁽³⁵⁾ Measurements of CPD can be used to obtain information concerning these parameters.

To achieve high lateral resolution, the Kelvin probe technique was modified to Kelvin force microscopy using the principles of AFM.⁽³⁵⁾ Various implementations of the KFM technique were developed in the past on the basis of using the gradient of the electrostatic force,⁽³⁶⁾ the second-harmonic resonance of the cantilever,⁽³⁸⁾ a broad resonance peak at low frequency,⁽⁴⁶⁾ phase detection,⁽⁴⁷⁾ and combination with local current detection.⁽⁴⁸⁾ Nowadays the most commonly used method seems to be a lift-mode technique,^(24,37,39) which is also employed in this work.

To obtain the absolute value of the potential, the work function of the cantilever probe must be calibrated on a reference sample with a known surface potential. In this study, gold surfaces were used. Their work function was determined by total photoyield experiments which enable access to values of both surface work functions and electron affinities.^(15,49)

KFM is typically performed on conductive or low-resistance samples to enable equilibration of Fermi energy levels between the sample and probe tip during the CPD measurement. On hydrogenated diamond surfaces, the surface region below the tip is connected to the ground via the surface conductive layer, and the conductive tip is biased with respect to the ground (see Fig. 1). Thus the main potential drop occurs across the gap between the tip and the surface. If the resistivity of other parts in the circuit (such as of the hydrogen-terminated surface and the cantilever probe) remains constant, the KFM potential profiles reflect the surface properties.

On highly resistive surfaces, such as oxidized diamond surfaces, CPD detection is done against a floating potential of the surface. Yet the KFM measurement is still possible because the probing voltage is applied to the conducting tip. Thus, with careful evaluation, information can be deduced from CPD profiles even on resistive surfaces.

2.4 AFM and KFM cantilever probes

For AFM and KFM measurements, common n-type doped silicon cantilevers were mainly used, with typical spring constants of 20–40 N/m, resonance frequencies of 190–320

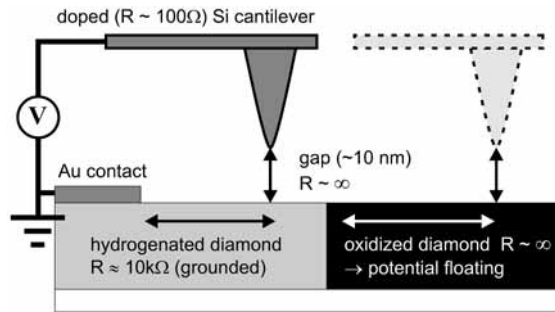


Fig. 1. Schematic setup of KFM on hydrogenated and oxidized diamond surfaces.

kHz, and a resistivity of $\approx 0.01 \Omega\text{cm}$. Their simple composition (doped silicon body covered by a natural silicon oxide layer) enables ease of use and straightforward interpretation of AFM and KFM measurements. In spite of being covered by silicon oxide, the silicon cantilevers provided good and reliable KFM images, because the oxide layer represents only an additional resistance in the tip-sample gap and as such does not influence relative contrast in KFM measurements.

Cantilevers coated by PtIr alloy (Pt 95%, Ir 5%) were used to corroborate KFM results obtained using the silicon cantilevers. The PtIr-coated cantilevers had a typical spring constant of 3 N/m and a resonance frequency of 75 kHz. The metal coating prevented photovoltage effects on the tip during KFM measurements under illumination. However, when using such tips, one has to be careful about possible inaccuracies in CPD values. Due to abrasion of the tip coating, the CPD can significantly change as the tip-sample distance decreases and the electrostatic interaction becomes more and more concentrated at the tip apex.^(50,51)

The type of applied cantilever influences the CPD values measured by KFM. For silicon AFM tips with a work function lower than the diamond samples used here, the CPD signal has negative polarity (see Fig. 2(a)). The opposite holds for metallized tips with higher work functions (see Fig. 2(b)). In both cases, brighter regions in KFM images correspond to relatively lower work functions.

3. Results and Discussions

Figure 3 shows AFM surface morphology and KFM potential images for samples which were grown and hydrogenated using the hot-filament CVD technique.

Figures 3(a)–3(c) show an image and profiles of surface morphology obtained by AFM across gold contact (Au), hydrogen-terminated (C-H), and plasma oxidized (C-O) surface regions. The white line in the AFM image indicates the position of the height profiles. In the image as well as in the profiles, a 50 nm step at the gold contact edge can be resolved along the left side. Height modulations on the diamond surface are generated by homoepitaxial deposition. Due to the surface corrugation, no difference between hydrogen-terminated and oxidized diamond could be resolved.

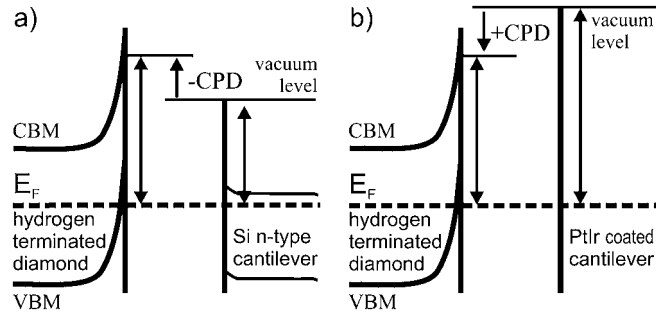


Fig. 2. Scheme of energetic bands in the KFM setup on diamond using (a) n-type silicon and (b) PtIr-coated cantilevers.

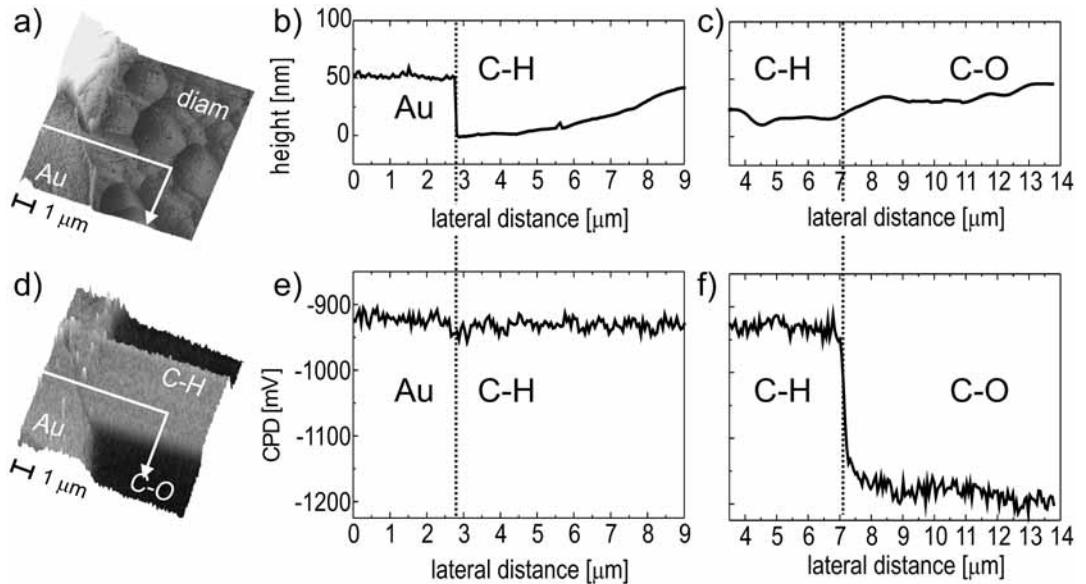


Fig. 3. Images and profiles across gold contact (Au), hydrogen-terminated (C-H), and oxidized (C-O) surface regions obtained by ((a)–(c)) AFM and ((d)–(f)) KFM using doped silicon tips.

Potential images and CPD profiles obtained by KFM at the same position are shown in Figs. 3(d)–3(f). The KFM measurements were done using plain silicon cantilevers. There is a clear contrast between hydrogen-terminated and oxidized parts. The bright region (the brightness of which is similar to the gold contact) is hydrogenated, whereas the darker areas correspond to oxidized diamond parts having a higher work function. It is noticeable that the CPD is identical (in the range of KFM precision) on Au and C-H surfaces.

For natural IIa diamonds, which were hydrogenated by the microwave plasma process, the image of surface morphology including aluminum and gold contacts is shown in Fig. 4(a). White lines indicate AFM line scans across aluminum and gold which are shown in Fig. 4(b). Corresponding images and spatial profiles of CPD obtained by KFM at the same place are displayed in Figs. 4(c) and 4(d). Here the KFM measurements were done using

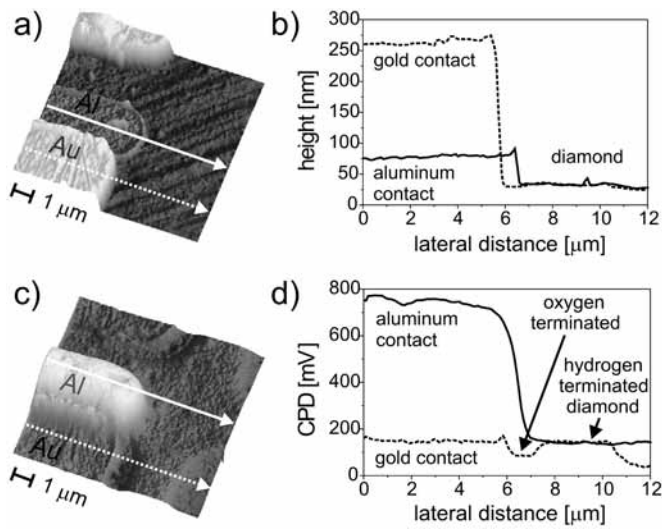


Fig. 4. (a) AFM morphology image and (b) height profiles of hydrogen-terminated diamond surface with aluminum and gold contacts (on the left side). (c) Corresponding KFM image and (d) potential profiles at the same place.

metal-coated cantilevers, which results in different CPD values compared to measurements with plain silicon cantilevers.

Nevertheless, just as on the hot-filament CVD samples, the surface potential of the hydrogen-terminated surface is the same as on gold. On the other hand, aluminum exhibits quite a large difference of 0.6 eV. The CPD contrast between aluminum and gold is due to a difference in their work functions, although they are on the same electrical potential (ground).

3.1 Deducing Fermi energy

In spite of different CPD values due to the use of silicon or metal-coated cantilevers, the CPD spatial profiles in Figs. 3 and 4 show that work functions of gold contact and hydrogenated diamond are identical on both types of samples.

Such CPD profiles can be used to deduce the Fermi energy at hydrogen-terminated diamond surfaces^(17,24) but the work function of gold and electron affinity of diamond must be obtained independently. In our case, the reference work function of the gold contacts was found to be 4.9 ± 0.1 eV using total photoyield experiments (as measured in the group of Prof. L. Ley, University of Erlangen-Nürnberg). This value is in a reasonable agreement with the 5.0 eV reported in the literature for polycrystalline gold.⁽⁵²⁾

Considering a typical negative electron affinity of $\chi = -1.3$ eV on hydrogen-terminated diamond^(5,49) and an energy band gap of $E_g = 5.5$ eV leads to the Fermi energy level 0.7 ± 0.1 eV below the valence band minimum at the hydrogen-terminated surface. This indicates a large accumulation of holes and strong band bending in the subsurface region as shown by the schematic diagram of energetic band profiles perpendicular to the hydrogen-terminated surface in Fig. 5(a).

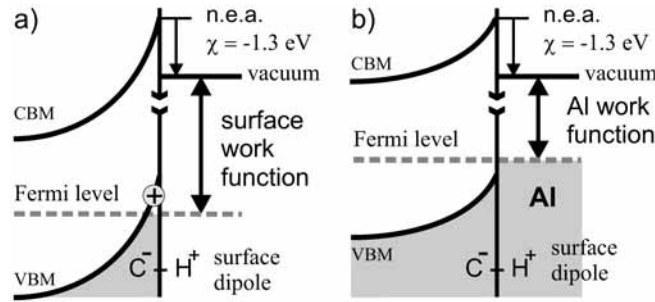


Fig. 5. Diagram showing energetic bands perpendicular to (a) hydrogen-terminated diamond surface as deduced from KFM profiles in Fig. 3 and to (b) hydrogen-terminated diamond surface below aluminum contact as deduced from KFM profiles in Fig. 4.

The precision of the Fermi energy value deduced from KFM depends on the resolution of KFM. On the fundamental level, the voltage resolution is limited by thermal oscillations of the cantilever. Thus, the resolution can be calculated as⁽³⁵⁾

$$V_{\min} = \left(\frac{2k_B T k_B}{\pi^3 Q f_{\text{res}}} \right)^{1/2} \frac{1}{\epsilon_0 V_{\text{ac}}} \frac{z}{R}. \quad (1)$$

Using typical parameters for silicon cantilevers and KFM measurements (see Table 1) the expected voltage resolution is $V_{\min} = 21$ mV. This is comparable to the fluctuations of ± 20 mV in the Au/C-H profile. With respect to the gold work function of 4.9 eV, these fluctuations are negligible. Although due to an inhomogeneity of a tip coating the CPD can also be a function of tip-sample distance in KFM,^(50,51) the results obtained for coated and uncoated cantilevers are in agreement in this case.

The absolute value of the Fermi level is determined by the reference work function of the gold contact and by the negative electron affinity of diamond. Exposure to ambient air may influence both those quantities.

The negative electron affinity of -1.3 eV used in our calculations was obtained for clean, hydrogen-terminated diamond surfaces in vacuum.^(5,49) The influence of surface chemical modifications and physisorption of adsorbates (in particular, water) in air is a matter of ongoing research.⁽⁵³⁾ Studies of dipole-oriented water layers on mica substrates reported a change of surface potential by 0.4 eV at room temperature and ambient humidity.⁽⁵⁴⁾ Taking this value into account, the Fermi level would lie 0.3 eV below VBM, under the rather strong assumption that water layers formed on mica and diamond have a similar configuration.

Nevertheless, the hydrogenated diamond as well as the gold surface (when exposed to air for some time) exhibit hydrophobic properties.⁽⁵⁵⁾ We presume that the dipole properties of the layer of adsorbed moisture may be similar on both surfaces and that its influence on the relative contrast in CPD will be minimal. This still has to be proven by further experiments.

Theoretical calculations using self-consistent solutions of the Schrödinger and Poisson equations revealed that the Fermi energy at the interface of hydrogen-terminated diamond

Table 1
Parameters used for calculation of KFM voltage resolution.

$f_{re} = 320 \text{ kHz}$	$Q = 300$
$k = 40 \text{ N/m}$	$V_{ac} = 0.5 \text{ V}$
$R = 10 \text{ nm}$	$B_{kfm} = 300 \text{ Hz}$
$z = 5 \text{ nm}$	$T = 293 \text{ K}$

and water should be in the range 0.3 to 0.9 eV below VBM.⁽¹⁸⁾ Thus, despite the uncertainty introduced by ambient conditions, both Kelvin probe experiments and theoretical calculations support the conclusion that the Fermi level on a hydrogen-terminated surface is rather deep in the valence band.

3.2 Hydrogenated surfaces and aluminum

Compared to the surface potentials on hydrogen-terminated diamond surfaces, which were the same as on gold, aluminum contacts exhibited a difference of 0.6 eV as can be seen in Fig. 4. Using the gold work function as a reference yields an aluminum work function of 4.3 eV, in agreement with literature values for polycrystalline aluminum.⁽⁵⁶⁾ Yet generally, the formation of aluminum oxide under ambient conditions can give rise to variations in this value. Thus aluminum is not optimal as a work function reference metal. Still it is attractive as a Schottky contact on hydrogenated diamond.⁽⁵⁷⁾

Considering the aluminum work function of 4.3 eV and the negative electron affinity of hydrogenated diamond (−1.3 eV), the Fermi level at the aluminum-diamond interface is coincident or only slightly above the VBM, with an accuracy of ± 0.1 eV given by the accuracy of the total photoyield experiments on gold. As shown by a schematic drawing of band profiles in Fig. 5(b), no hole accumulation is generated in this case below the aluminum layer at zero bias voltage, thus giving rise to Schottky behavior of the aluminum contact.

On the basis of these deductions, lateral hole depletion regions are also expected next to the aluminum contacts. Previous studies using capacitance-voltage characteristics indicated depletion regions 0.5–100 nm wide.⁽⁵⁷⁾ Here, KFM was applied to investigate such lateral depletion profiles. Typical profiles of surface potential and surface height across the aluminum Schottky junction are displayed in Fig. 6.

The potential on diamond decays across several micrometers in the lateral direction from the contact edge. This indicates a wide depletion region. However, the potential profile as measured by KPM is given not only by band bending in the depletion region but also by the edge transfer function⁽³⁷⁾ which is determined by the capacitance contributions from the tip apex, tip body, as well as cantilever plate (see Fig. 7(a)) and which may spread over several micrometers.

The spatial resolution is also limited by the shape of the AFM tip and by the height of the aluminum contact.⁽²²⁾ This situation is schematically depicted in Fig. 7(b). A region at the very edge of the contact may be inaccessible for measurement because of the AFM tip shape. The width of the inaccessible region x can be estimated from geometry using $x = h \tan(\alpha/2)$. Substituting $h = 45 \text{ nm}$ for height at the contact edge and $\alpha = 50^\circ$ for the opening angle of the tip apex gives the width of the region as $x = 21 \text{ nm}$.

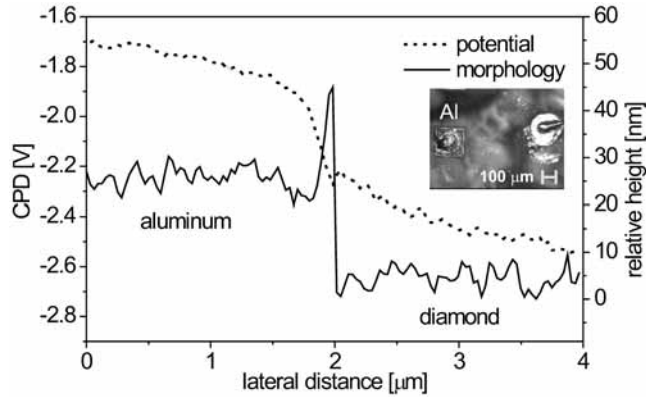


Fig. 6. Lateral morphology (solid) and potential (dashed) profiles across an aluminum Schottky junction.

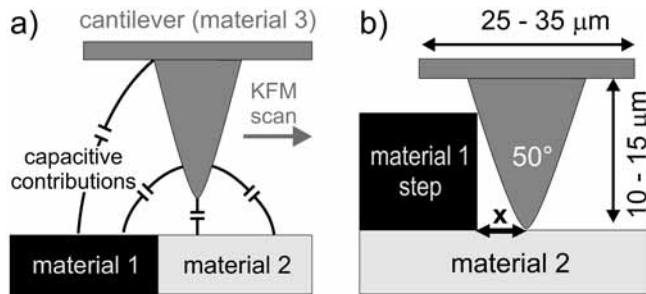


Fig. 7. (a) Scheme of capacitance contributions from AFM cantilever to the KFM measurement. (b) Scheme of AFM cantilever tip at the contact edge.

The inaccessible region and the edge transfer function spreading over a few micrometers make unambiguous evaluation of the depletion regions at aluminum Schottky junctions from the above potential profiles difficult.

3.3 Hydrogenated and oxidized surfaces

On the basis of the CPD profiles in Fig. 3 and the previous discussion, a schematic model of lateral energetic band profiles across the Au/C-H/C-O surface regions can be assembled. It is presented in Fig. 8.

In the drawing, the surface Fermi level is aligned in all Au, C-H, and C-O regions. Across the conductive Au and C-H surfaces the alignment is achieved by charge carrier diffusion in a straightforward manner. At the highly resistive C-O surface, the Fermi level cannot be so readily established and the straight level is only a schematic image. In the measured CPD profile (see Fig. 3(f)), there is a weak yet noticeable slope across the C-O region compared with the straight profile in the C-H region. This slope is due to an effect of the floating potential of the highly resistive C-O surface.

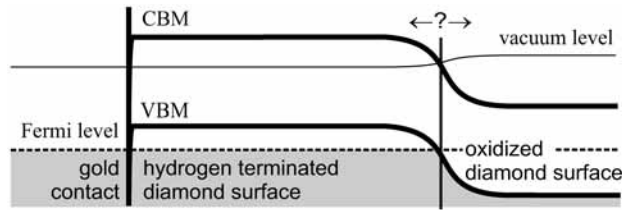


Fig. 8. Scheme of energetic bands profiles across Au, C-H and C-O surfaces, assembled on the basis of KFM profiles in Fig. 3.

The position of the Fermi level within the band gap is generally not obvious. KFM data in Fig. 3(f) indicate that at the C-O surface the vacuum level is 0.3 eV higher than at the C-H surface. Taking into account a range of positive electron affinities observed on oxidized diamond surfaces puts the Fermi level approximately 0.7–2.0 eV above the valence band maximum. This assumes pinning of the Fermi level there in some surface or defect states. The pinning provides a good foundation for the Fermi level alignment and KFM evaluation at this highly resistive region. Detailed discussion of the band gap states including a study under illumination follows in § 3.4.

Note that the position of the C-H/C-O boundary could not be resolved from the height profile in Fig. 3(c). Therefore, the position of C-H/C-O boundary cannot be correlated with the potential profile in this case.

Properties of the C-H/C-O interface were investigated by AFM/KFM also on the inplane transistor structures, which were prepared on MW-CVD samples by electron beam lithography and oxygen plasma treatments. The resulting lateral profiles are displayed in Fig. 9.

Across the two oxidized line shapes (gray), which were generated by the oxygen plasma process, the CPD increases to more negative values. This increase corresponds to a higher work function of the C-O surface. As shown in the inset, the transistor channel was grounded and both gates were symmetrically biased.⁽²²⁾ In this case, the gate bias $V_G = 0.2$ V. This resulted in a potential difference between the C-H gate leads (side regions) and the C-H channel (central region).

In the AFM profile, the two oxidized lines can be resolved by a slight increase in height of 1 nm. The origin of this height increase is unclear, although some explanations have been proposed, for instance in ref. 20. Due to the height difference, the extent of the oxidized regions can be identified here from the morphology profile (denoted by the vertical black lines in Fig. 9), and they can be directly correlated with the potential profile.

It is remarkable that the potential across the C-H/C-O boundary changes only within the oxidized regions. In the C-O region it exhibits a pronounced decrease within 1 μm from the boundary (as observed also in Fig. 3(f)). In the surrounding hydrogenated regions it remains constant. This allows some information to be deduced about the depletion regions at the C-H/C-O interface.

First, the depletion width in the C-H region must be very narrow, below the KFM lateral resolution. The lateral KFM resolution can be estimated as $5z$ for tip-surface distances z greater than 3 nm,⁽⁴⁰⁾ i.e., a resolution of 25–50 nm is expected for typical separations of z

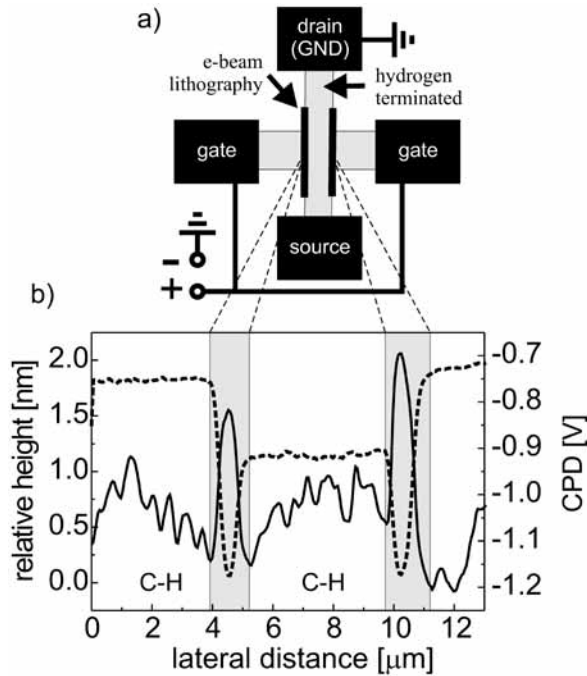


Fig. 9. AFM (solid) and KFM (dashed) profiles across the in-plane transistor structure comprising hydrogen-terminated (C-H) and oxidized (gray) regions. The inset shows the device scheme.

= 5–10 nm. Such narrow depletion regions on C-H surfaces were deduced also from current-voltage characteristics of in-plane gate transistors.⁽⁵⁸⁾ The resolution of AFM/KFM at the C-H/C-O interface is not influenced by a step in height. For the step in height of 1 nm the region inaccessible by the AFM tip has a negligible width of <1 nm.

Second, the change of potential across 1 μm in the C-O region suggests a wide space charge region. Previously, such potential decay across several micrometers from the material boundary were attributed to a stray capacitance of the cantilever.^(22,37) In those cases the potential profile was symmetrical with respect to the boundary. This is not the case here. Hence the decay may be related to hole trapping at surface or defect states near the C-H/C-O interface.

3.4 KFM under illumination

Electronic properties of band gap states can be probed by sub-band-gap illumination.⁽⁵⁹⁾ The potential variations at hydrogenated and oxidized surfaces as measured by KFM using a bias light (visible wavelength range) are shown in Fig. 10(a). The inset displays the KFM image of the interface region between the C-O and C-H surfaces as a function of illumination. In the course of KFM scanning, the conditions were varied from dark to weak to intense illumination by a broadband white light (from bottom to top). Corresponding line profiles show a change of potential in both C-O and C-H regions. On the C-H surface, the illumination results in a decrease in CPD by as much as 0.2 V in the case of intense

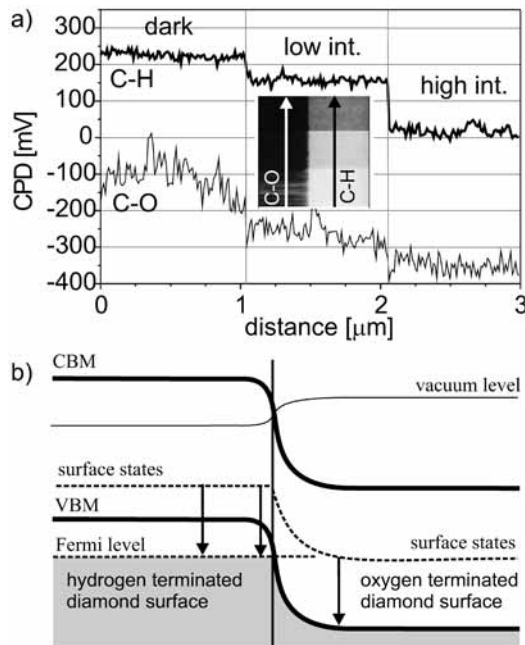


Fig. 10. (a) CPD on hydrogenated and oxidized diamond surfaces as a function of illumination (using metal coated tips). The inset shows the KFM image in the same region; the arrows denote the position and direction of the profiles. (b) Schematic model of energetic band profiles across the C-H/C-O interface including the energetic level of the surface states. The arrows denote excitation of holes from these states by sub-band-gap illumination.

illumination. The trend is similar on the C-O surface, but there it corresponds to an increase in CPD to more negative values. Note that although the C-O surface is highly resistive, the relative changes can still be detected by KFM.

The change of potential during illumination is referred to as the surface photovoltage effect.⁽⁵⁹⁾ Contrast may arise from a change in the total surface charge or from modification of carrier transport kinetics in the subsurface region. Both the surface charge and transport kinetics are also influenced by defects and other surface inhomogeneities.

In this particular case, the surface photovoltage effect gives rise to increased band bending on both C-H and C-O surfaces. For a sub-band-gap light energy, this effect must be facilitated by excitation of holes from some surface or defect states within the band gap.⁽⁵⁹⁾ Its mechanism is shown in Fig. 11. The energy of visible light suggests that these states are lower than 3 eV above the VBM. The energetic level of the band gap states is depicted in a scheme of energetic band profiles across the C-H/C-O interface in Fig. 10(b). The arrows denote the possible excitation of trapped holes by sub-band-gap illumination. Note that this is only a schematic picture because the surface states are most likely distributed over more than a single energetic level.

Previously, band gap donorlike states were indicated 1.7 eV above the VBM on oxidized undoped CVD diamond films using X-ray photoelectron spectroscopy analysis.⁽¹⁰⁾ Current-

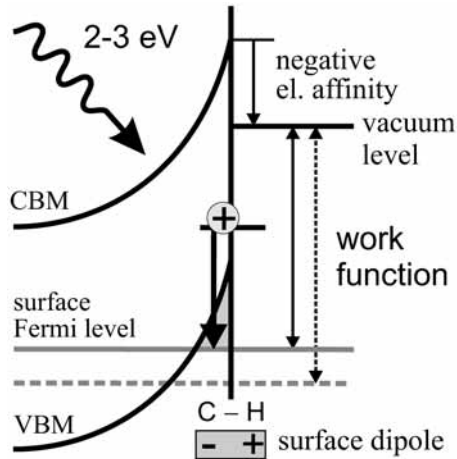


Fig. 11. Mechanism of the surface photovoltage effect under sub-band-gap illumination on hydrogen-terminated diamond surfaces.

voltage measurements of Schottky junctions on oxidized B-doped diamond films revealed three pinning states 1.2–1.3 eV, 1.7 eV and 2.1 eV above the VBM.⁽⁶⁰⁾ On in-plane gate field-effect transistors (FET) comprised of hydrogen-terminated (conductive) and oxidized (nonconductive) patterns on undoped diamond films, hysteresis of channel current as a function of gate voltage was attributed to photoexcitation of holes from surface defects on oxidized regions, with the energy of 2.2 eV above the VBM.⁽⁶¹⁾ Spectrally resolved photocurrents on similar structures showed an absorption peak around 3.1 eV.⁽⁷⁾ Total photoyield experiments on both hydrogen-terminated and oxidized B-doped diamond deduced energetic states about 0.3 eV above the VBM due to surface defects or graphitic patches.^(15,62)

All the surface states proposed previously fall within the energetic range of the broadband visible light applied here. In the case of in-plane FETs the spatial KFM potential profiles indicate that holes from the C-H channel can be trapped and detrapped at least 1 μm far in the C-O region and thus can contribute to the absorption peaks and hysteresis in the photocurrents. More details about energetic and spatial distribution of particular surface states on hydrogen-terminated and oxidized diamond surfaces could be gained in the future by KFM under spectrally resolved illumination.

3.5 Effect of plasma hydrogenation

The above characteristics of hydrogenated diamond surfaces depend inherently on their microstructure. Applying noncontact AFM after exposure of diamond to hydrogen plasma revealed inhomogeneous surface morphologies. Figure 12(a) displays a typical image obtained by nc-AFM after a smaller rectangular area inside was scanned by c-AFM where a silicon probing tip was pressed against the surface with a force of 0.1–1 μN during scanning. The surrounding original surface is covered by fine hillocks (<100 nm width, RMS roughness 1.1 nm) and also several line-shaped features can be noticed. In contrast, the area scanned by c-AFM appears flatter and smoother (RMS roughness 0.2 nm). A line

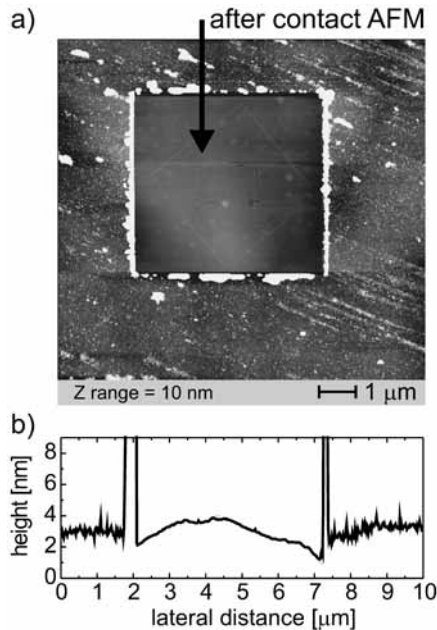


Fig. 12. (a) Surface morphology obtained by noncontact AFM after scanning the central area by contact AFM. (b) Height profile across the central area.

profile across this area is shown in Fig. 12(b), which reveals that some material was swept aside by c-AFM scanning. From the line profile, its thickness was evaluated as ≈ 1 nm. On the basis of XPS spectra, this material may be attributed to a carbon deposit generated during a plasma cooling process. It is important to note that this deposit was not the origin of a high surface conductivity. After its removal, the surface conductivity remained about the same.

We have applied KFM to characterize surface potentials of as-hydrogenated and cleaned areas. Figure 13(a) shows the nc-AFM surface morphology of the as-hydrogenated surface. A rough surface morphology, typical for the deposit, can be resolved there. Figure 13(b) shows the nc-AFM surface morphology after scanning the central area by c-AFM. There the uncovered surface appears cleaner than the original surface along the top and bottom edges of the image. The image of surface potentials of the same area is shown in Fig. 13(c). There the brighter KFM image corresponds to a lower work function (as discussed previously). The cleaned surface exhibits a work function about 80 mV lower than the original surface covered by the carbon deposit. This can be attributed to a higher negative electron affinity of the cleaned surface. This was confirmed by the contrast observed in SEM where the areas cleaned by c-AFM showed enhanced electron emission (see Fig. 14).

The electronic properties of as-hydrogenated and mechanically cleaned surfaces indicate that the hydrogen-terminated surface is in fact beneath a very thin carbon deposit layer. This assertion was also corroborated by wetting angle experiments showing an increase in wetting angles on cleaned surfaces.⁽⁶³⁾

To avoid an influence of the carbon deposit, the surfaces were scanned by c-AFM prior to the KFM measurements in this study.

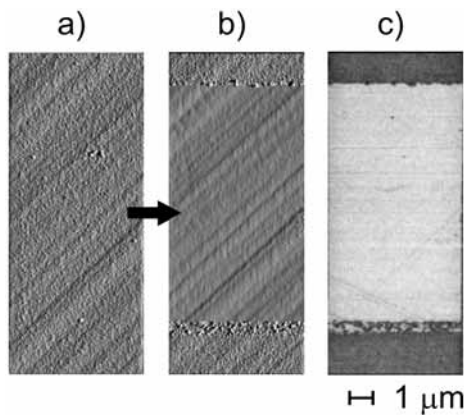


Fig. 13. Noncontact AFM surface morphology of (a) an as-hydrogenated surface and (b) after scanning the central area by contact AFM. (c) The image of surface potentials obtained by KFM on the same area. A brighter area corresponds to a lower work function.

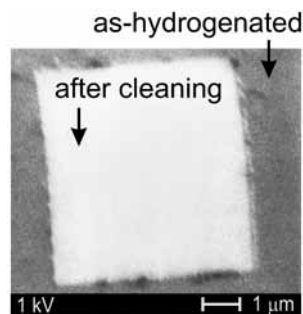


Fig. 14. SEM image of the area scanned previously by contact AFM.

3.6 AFM-induced surface modifications

AFM can be used not only to characterize but also to modify electronic as well as structural properties of hydrogenated diamond surfaces on a microscopic level. Using AFM in the contact mode, the hydrogen termination of a diamond surface was removed by applying negative bias voltages to doped silicon AFM cantilevers. This gave rise to the formation of insulating patterns which appeared scribed into the diamond surface.⁽²¹⁾

The typical surface morphology of a pattern prepared by AFM oxidation is shown in Fig. 15(a). The image was obtained using AFM in the contact mode. A trench scribed into the flat and smooth diamond surface is detected. It is worth emphasizing that common silicon tips (biased at -10 V) were used in this procedure. The line profile shows that the depth of the trench is 0.3 nm. Along the trench, the depth varies between 0.1 – 0.6 nm. The width of the trench at half maximum is about 60 nm. In general, the width can be controlled by adjustment of the bias voltage.^(19,22) In a special case, the inscribed pattern was as deep as 3.4 nm at the same bias voltage.⁽²¹⁾ The difference in depth is most likely related to the shape and quality of the specific AFM tip used.

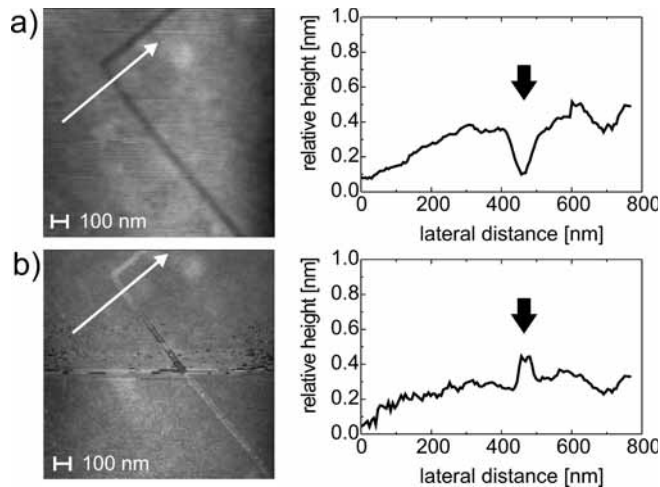


Fig. 15. (a) Contact and (b) noncontact AFM morphologies of a pattern inscribed into the hydrogenated diamond surface by AFM. In the noncontact AFM image, the shift from height to depth profile can be observed.

Changing the AFM mode of operation to noncontact (the cantilever resonance frequency was about 320 kHz), the pattern looks as if it was deposited onto the surface with a thickness of about 0.2 nm. This is illustrated by Fig. 15(b), showing nc-AFM images of the same pattern. The transition from a height to depth profile can be noticed as the cantilever was brought closer to the surface by adjustment of the set-point during nc-AFM scanning. Such effects can be attributed to switching between attractive and repulsive tip-surface interactions controlling the measurement in the noncontact mode.^(64,65)

Now the question arises: what is the real structure? The true surface morphology is revealed when the tip touches the surface and stronger repulsive forces dominate the interaction. This is the case in the contact mode and also in the so-called tapping mode AFM. In the noncontact mode, the interaction between the tip and the sample is small and the cantilever is very sensitive to long-range forces. Two factors may influence the height contrast.

First, cantilever oscillations can be influenced by a different electrostatic potential above the oxidized pattern and the surrounding hydrogenated surface because oxidation changes the electron affinity and increases the total work function of diamond.⁽⁴⁹⁾ A larger work function difference between the oxidized surface and the cantilever gives rise to a larger electrostatic interaction, which can result in apparent height contrast in the morphological image.⁽⁶⁶⁾

Second, moisture may be preferentially adsorbed on the oxidized patterns because of their hydrophilic properties compared with the hydrophobic properties of the surrounding hydrogenated surface.⁽⁶⁷⁾ This also can lead to a variation of surface height. In ambient humidity (33–37%), a typical thickness of the moisture layer is in the order of 0.1 nm,⁽⁶⁸⁾ which agrees well with the observed height difference on the oxidized (hydrophilic) patterns. While in our opinion this effect is dominating, conclusive interpretation requires further research.

The AFM scribing into diamond affects not only the morphology but also the electronic properties at the surface. Figure 16 shows I-V characteristics measured using an AFM tip as a local contact. The measurement setup is schematically illustrated in the inset in Fig. 16. When the tip is inside the square, the I-V characteristics are controlled by electronic transport through the oxidized barrier. Note that currents at negative bias are smaller than those at positive tip voltages, because the onset of oxidation around -4 V affects the measurement. I-V characteristics measured outside the insulating pattern are ohmic and show larger conductivity by more than three orders of magnitude, in agreement with macroscopic measurements on hydrogenated diamond surfaces.

3.7 Device examination

Combination of the AFM oxidation process and KFM can be used for in situ visualization and adjustment of electronic device structures, such as in-plane gate transistors. This is demonstrated on an in-plane gate transistor which was prepared by electron beam lithography on hydrogenated diamond.⁽²²⁾

The schematic design of this device is displayed in Fig. 17(a). Figure 17(b) shows the CPD image obtained with KFM on the device as-prepared by electron beam lithography.

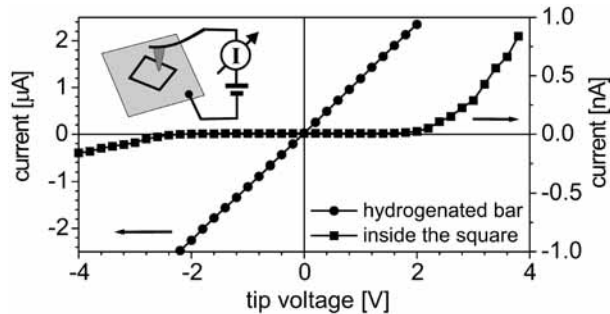


Fig. 16. Current-voltage characteristics measured with the AFM tip from inside the AFM scribed pattern (squares) and on the hydrogenated surface outside the pattern (circles). The setup is shown schematically in the inset.

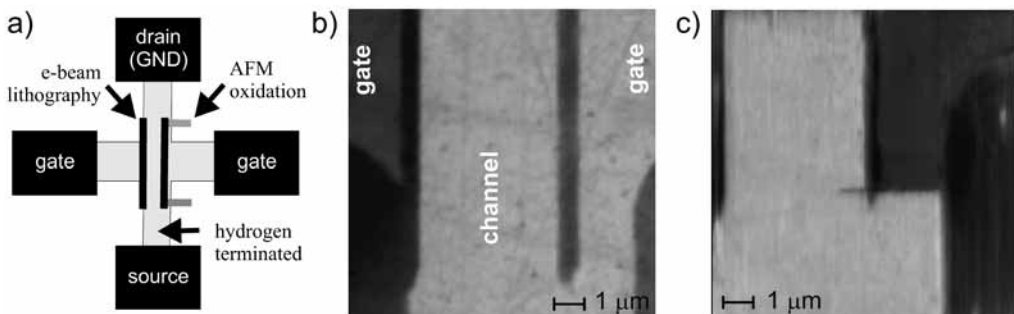


Fig. 17. (a) Schematic design of in-plane gate transistor on diamond. KFM image of the transistor channel (b) after electron beam lithography (the right gate is leaking) and (c) after the leak was corrected in situ using AFM-induced oxidation.

The hydrogenated channel appears bright. There are two parallel oxidized lines (darker), the width of which is about 500 nm (ensuring their good electrical insulation). Yet, as indicated by the potential image, the left line insulates the gate well, while the right line is obviously misaligned. Figure 17(c) shows a potential image of the same place after the leakage of the right gate was corrected in situ by local oxidation using AFM.

4. Summary

To summarize, AFM and KFM were used to characterize the morphology and electronic properties of diamond surfaces. Potential images obtained by KFM clearly resolved hydrogen-terminated and oxidized regions. The Fermi energy level on the hydrogen-terminated surfaces could be determined by comparison of potential profiles across the Au/C-H junction. Its energy was estimated below the valence band minimum, thereby indicating strong accumulation of holes near the hydrogen-terminated surface. Determination of the Fermi energy relied on independent measurements of diamond electron affinity and calibration of the gold work function by total photoyield experiments. Evaluation of CPD across aluminum contacts indicated that no hole accumulation layer is generated below the contacts, thereby explaining their Schottky characteristics.

Evaluation of CPD profiles across oxidized surface regions and their correlation with the C-H/C-O boundary implied the presence of band gap states and trapping of holes there. This assertion was confirmed by KFM measurements of the surface photovoltage effect under sub-band-gap illumination, which indicated band gap states also within hydrogenated regions.

Electronic as well as structural properties of hydrogenated diamond surfaces were modified on the microscopic level using negatively biased AFM cantilevers. By this technique, nanoscale patterns were inscribed into the diamond surface. Preferential adsorption of air moisture on these patterns was proposed on the basis of comparison of c-AFM and nc-AFM measurements. Conductivity through these patterns was several orders of magnitude lower than on the hydrogen-terminated surfaces. In combination with KFM, the AFM patterning was used for in situ examination and adjustment of in-plane gate transistor structures realized on diamond.

By providing an invaluable insight into the unique properties of diamond, the AFM and KFM techniques can contribute to understanding, improving, and initiating new concepts for diamond-based devices.

Acknowledgments

The author would like to gratefully acknowledge the kind support of Prof. Martin Stutzmann and Dr. Christoph E. Nebel as well as fruitful cooperation with Dr. J. A. Garrido at the Walter Schottky Institut, Technical University Munich, Germany. Collaboration with research groups of Prof. L. Ley at the University of Erlangen-Nürnberg, Germany, Dr. P. Bergonzo at the CEA/Saclay, France, and Dr. H. Okushi at the Diamond Research Center of AIST, Tsukuba, Japan, is greatly appreciated. This research has been financed by the European Community contract HPRN-CT-1999-00139, Deutsche Forschungsgemeinschaft contract NE524-2, and the Procope French-German program.

References

- 1) S. Yamanaka, H. Watanabe, S. Masai, D. Takeuchi, H. Okushi and K. Kajimura: Jpn. J. Appl. Phys. **37** (1998) L1129.
- 2) S. Koizumi, M. Kamo, Y. Sato, H. Ozaki and T. Inuzuka: Appl. Phys. Lett. **71** (1997) 1065.
- 3) M. I. Landstrass and K. V. Ravi: Appl. Phys. Lett. **55** (1989) 975.
- 4) F. J. Himpsel, J. A. Knapp, J. A. van Vechten and D. E. Eastman: Phys. Rev. B **20** (1979) 624.
- 5) F. Maier, J. Ristein and L. Ley: Phys. Rev. B **64** (2001) 65411.
- 6) K. Tsugawa, K. Kitatani, H. Noda, A. Hokazono, M. Tajima and H. Kawarada: Diamond Relat. Mater. **8** (1999) 927.
- 7) J. A. Garrido, C. E. Nebel, R. Todt, M. C. Amann, O. A. Williams, R. Jackman, M. Nešládek and M. Stutzmann: Phys. Status Solidi A **199** (2003) 56.
- 8) H. Kawarada, Y. Araki, T. Sakai, T. Ogawa and H. Umezawa: Phys. Status Solidi A **185** (2001) 79.
- 9) A. Härtl, E. Schmich, J. A. Garrido, J. Hernando, S. C. R. Catharino, S. Walter, P. Feulner, A. Kromka, D. Steinmüller and M. Stutzmann: Nature Mater. **3** (2004) 736.
- 10) J. Shirafuji and T. Sugino: Diamond Relat. Mater. **5** (1996) 706.
- 11) K. Hayashi, S. Yamanaka, H. Watanabe, T. Sekiguchi, H. Okushi and K. Kajimura: J. Appl. Phys. **81** (1997) 744.
- 12) A. Denisenko, A. Aleksov, A. Pribil, P. Gluche, W. Ebert and E. Kohn: Diamond Relat. Mater. **9** (2000) 1138.
- 13) S. G. Ri, T. Mizumasa, Y. Akiba, Y. Hirose, T. Kurosu and M. Iida: Jpn. J. Appl. Phys. **34** (1995) 5550.
- 14) F. Maier, M. Riedel, B. Mantel, J. Ristein and L. Ley: Phys. Rev. Lett. **85** (2000) 3472.
- 15) D. Takeuchi, M. Riedel, J. Ristein and L. Ley: Phys. Rev. B **68** (2003) 041304(R).
- 16) E. Snidero, D. Tromson, C. Mer, P. Bergonzo, J. S. Foord, C. Nebel, O. A. Williams and R. B. Jackman: J. Appl. Phys. **93** (2003) 2700.
- 17) B. Rezek, C. Sauerer, C. E. Nebel, M. Stutzmann, J. Ristein, L. Ley, E. Snidero and P. Bergonzo: Appl. Phys. Lett. **82** (2003) 2266.
- 18) C. E. Nebel, B. Rezek and A. Zrenner: Phys. Status Solidi A **201** (2004) 2432.
- 19) M. Tachiki, T. Fukuda, K. Sugata, H. Seo, H. Umezawa and H. Kawarada: Jpn. J. Appl. Phys. **39** (2000) 4631.
- 20) M. Tachiki, Y. Kaibara, Y. Sumikawa, M. Shigeno, T. Banno, K. S. Song, H. Umezawa and H. Kawarada: Phys. Status Solidi A **199** (2003) 39.
- 21) B. Rezek, C. Sauerer, J. Garrido, C. E. Nebel, M. Stutzmann, E. Snidero and P. Bergonzo: Appl. Phys. Lett. **82** (2003) 3336.
- 22) B. Rezek, J. Garrido, C. E. Nebel, M. Stutzmann, E. Snidero and P. Bergonzo: Phys. Status Solidi A **193** (2002) 523.
- 23) R. García, M. Calleja and F. Pérez-Murano: Appl. Phys. Lett. **72** (1998) 2295.
- 24) B. Rezek, C. E. Nebel and M. Stutzmann: Diamond Relat. Mater. **13** (2004) 740.
- 25) C. E. Nebel: Nature Mater. **2** (2003) 431.
- 26) N. Jiang and T. Ito: J. Appl. Phys. **85** (1999) 8267.
- 27) O. A. Williams and R. B. Jackman: Semicond. Sci. & Technol. **18** (2003) S34.
- 28) R. Wiesendanger and H. J. Güntherodt (Eds.): *Scanning Tunneling Microscopy I, Vol. 20 of Springer Series in Surface Sciences* (Springer, Berlin, 1992).
- 29) R. Wiesendanger, H. J. Güntherodt (Eds.): *Scanning Tunneling Microscopy II, Vol. 28 of Springer Series in Surface Sciences* (Springer, Berlin, 1992) p. 99.
- 30) B. Rezek, T. Mates, J. Stuchlík, J. Kočka and A. Stemmer: Appl. Phys. Lett. **83** (2003) 1764.
- 31) T. Tsuno, T. Imai, Y. Nishibayashi, K. Hamada and N. Fujimori: Jpn. J. Appl. Phys. **30** (1991) 1063.

- 32) J. Nakamura, S. Fukumoto, T. Teraji, H. Murakami and T. Ito: Appl. Surf. Sci. **216** (2003) 59.
- 33) R. García and A. S. Paulo: Surf. Sci. Rep. **47** (2002) 197.
- 34) B. Rezek, J. Stuchlík, A. Fejfar and J. Kočka: J. Appl. Phys. **92** (2002) 587.
- 35) M. Nonnenmacher, M. P. O'Boyle and H. K. Wickramasinghe: Appl. Phys. Lett. **58** (1991) 2921.
- 36) S. Kitamura and M. Iwatsuki: Appl. Phys. Lett. **72** (1998) 3154.
- 37) H. O. Jacobs, P. Leuchtman, O. J. Homan and A. Stemmer: J. Appl. Phys. **84** (1998) 1168.
- 38) C. Sommerhalter, T. W. Matthes, T. Glatzel, A. Jäger-Waldau and M. C. Lux-Steiner: Appl. Phys. Lett. **75** (1999) 286.
- 39) S. V. Kalinin and D. A. Bonnell: Phys. Rev. B **62** (2000) 10419.
- 40) P. Girard: Nanotechnology **12** (2001) 485.
- 41) A. Kikukawa, S. Hosaka and R. Imura: Appl. Phys. Lett. **66** (1995) 3510.
- 42) H. Sugimura, T. Hanji, K. Hayashi and O. Takai: Adv. Mater. **14** (2002) 524.
- 43) K. J. Kwak, S. Yoda and M. Fujihira: Appl. Surf. Sci. **210** (2003) 73.
- 44) B. Rezek and C. E. Nebel: Diamond Relat. Mater. **14** (2005) 466.
- 45) J. K. Arch and S. J. Fonash: J. Appl. Phys. **68** (1990) 591.
- 46) A. Breymesser, V. Schlosser, D. Peiró, C. Voz, J. Bertomeu, J. Andreu and J. Summhammer: Sol. Energy Mater. Sol. Cells **66** (2001) 171.
- 47) T. Takahashi and T. Kawamukai: Ultramicroscopy **82** (2000) 63.
- 48) B. Rezek, T. Mates, J. Stuchlík, A. Fejfar and J. Kočka: J. Non-Cryst. Solids **299–302** (2002) 360.
- 49) J. B. Cui, J. Ristein and L. Ley: Phys. Rev. Lett. **81** (1998) 429.
- 50) H. O. Jacobs, H. F. Knapp and A. Stemmer: Rev. Sci. Instrum. **70** (1999) 1756.
- 51) C. Sommerhalter, T. W. Matthes, T. Glatzel, A. Jäger-Waldau and M. C. Lux-Steiner: Appl. Surf. Sci. **157** (2000) 263.
- 52) S. M. Sze: *Physics of Semiconductor Devices*, 2nd ed. (John Wiley & Sons, New York, 1981).
- 53) G. Piantanida, A. Breskin, R. Chechik, O. Katz, A. Laikhtman, A. Hoffman and C. Coluzza: J. Appl. Phys. **89** (2001) 8259.
- 54) H. Bluhm, T. Inoue and M. Salmeron: Surf. Sci. **462** (2000) L599.
- 55) T. Smith: J. Colloid Interface Sci. **75** (1980) 51.
- 56) G. Chiarotti (Ed.): *Landolt-Börnstein New Series III/24b* (Springer, Berlin, 1994).
- 57) J. A. Garrido, C. E. Nebel, M. Stutzmann, E. Snidero and P. Bergonzo: Appl. Phys. Lett. **81** (2002) 637.
- 58) M. Tachiki, H. Seo, T. Banno, Y. Sumikawa, H. Umezawa and H. Kawarada: Appl. Phys. Lett. **81** (2002) 2854.
- 59) L. Kronik and Y. Shapira: Surf. Interface Anal. **31** (2001) 954.
- 60) D. Takeuchi, S. Yamanaka, H. Watanabe and H. Okushi: Phys. Status Solidi A **186** (2001) 269.
- 61) Y. Sumikawa, T. Banno, K. Kobayashi, Y. Itoh, H. Umezawa and H. Kawarada: Appl. Phys. Lett. **85** (2004) 139.
- 62) J. B. Cui, J. Ristein and L. Ley: Phys. Rev. B **60** (1999) 16135.
- 63) B. Rezek and C. E. Nebel: Diamond Relat. Mater. (submitted).
- 64) A. Kühle, A. H. Sørensen, J. B. Zandbergen and J. Bohr: Appl. Phys. A **66** (1998) S329.
- 65) R. García and A. S. Paulo: Phys. Rev. B **60** (1999) 4961.
- 66) T. Shiota and K. Nakayama: Jpn. J. Appl. Phys. **40** (2001) L986.
- 67) K. Larsson, H. Bjorkman and K. Hjort: J. Appl. Phys. **90** (2001) 1096.
- 68) M. Luna, J. Colchero and A. M. Baró: Appl. Phys. Lett. **72** (1998) 3461.